Published in final edited form as:
Comput Methods Programs Biomed. 2010 June ; 98(3): 223–230. doi:10.1016/j.cmpb.2009.09.001.

Real-time segmentation by Active Geometric Functions

Qi Duan[a,c,*], **Elsa D. Angelini**[b], and **Andrew F. Laine**[a]

[a] Department of Biomedical Engineering, Columbia University, ET-351, 1210 Amsterdam Avenue, New York, NY 10027, USA

[b] Department of Image and Signal Processing, Institut Telecom, Telecom ParisTech, CNRS LTCI, France

[c] Department of Radiology, NYU School of Medicine, New York, NY, USA

Abstract

Recent advances in 4D imaging and real-time imaging provide image data with clinically important cardiac dynamic information at high spatial or temporal resolution. However, the enormous amount of information contained in these data has also raised a challenge for traditional image analysis algorithms in terms of efficiency. In this paper, a novel deformable model framework, Active Geometric Functions (AGF), is introduced to tackle the real-time segmentation problem. As an implicit framework paralleling to level-set, AGF has mathematical advantages in efficiency and computational complexity as well as several flexible feature similar to level-set framework. AGF is demonstrated in two cardiac applications: endocardial segmentation in 4D ultrasound and myocardial segmentation in MRI with super high temporal resolution. In both applications, AGF can perform real-time segmentation in several milliseconds per frame, which was less than the acquisition time per frame. Segmentation results are compared to manual tracing with comparable performance with inter-observer variability. The ability of such real-time segmentation will not only facilitate the diagnoses and workflow, but also enables novel applications such as interventional guidance and interactive image acquisition with online segmentation.

Keywords

Active Geometric Functions (AGF); Deformable model; Real-time segmentation; Cardiac imaging

1. Introduction

Image segmentation is a critical step for quantitative image analysis. In medical imaging, image segmentation is the prerequisite for quantitative evaluation of organs and pathologies morphologies and diagnosis. For example, in cardiac imaging, delineating borders of

[*] *Corresponding author at*: 660 1st Ave. FL1, New York, NY 10016, USA. Tel.: +1 212 263 6643; fax: +1 212 263 7541. Qi.Duan@nyumc.org (Q. Duan)..

Conflict of interest statement
All authors in this paper have no potential conflict of interests.

chambers of the heart and valves are of great clinical importance. Segmentation of the left ventricular endocardium is required for quantitative evaluation of the LV function, such as ejection fraction or 3D fractional shortening [1]. With recent advances in 3D and 4D imaging techniques towards real-time imaging, the amount of data is becoming prohibitively overwhelming. Manual tracing of these large data sets is tedious and impractical in clinical setting.

In this context, automated or semi-automated segmentation methods have been proposed and applied to medical image analysis to leverage the human efforts involved in the segmentation task. Based on the mathematical foundation of each method, segmentation approaches can be roughly divided into several classes: classification (e.g. thresholding, *k*-means), region growing (such as fuzzy connectedness [2]), deformable models (e.g. snake [3], level-set [4–7]), active shape [8] and active appearance models [9], and probabilistic methods (Markov random field [10], graph cut [11]). Hybrid methods [12] combining different existing methods were also proposed. Among segmentation methods, deformable models are still widely used in medical image analysis, especially for cardiac imaging.

The first deformable model parametric formulation was proposed by Kass et al. in 1987 [3]. In 1998, Xu and Prince [13] proposed the Gradient Vector Flow (GVF) method to overcome several drawbacks in the original snake framework. In order to handle topological changes, especially in 3D, in the late 1990s, Sethian [14] proposed level-set framework by utilizing level-set functions with higher dimensionality than the data. In 2001, Chan and Vese [6] proposed their famous “active contour without edges”. The driving forces were derived via energy minimization of the Mumford–Shah segmentation functional [15]. Their method was widely used in ultrasound segmentation [16], brain segmentation [17], and many other applications. However, the introduction of level-set functions implicitly increased the number of parameters of the surface model, which increases the demand for computational power. Although many optimization modifications such as narrow-banding or fast marching schemes were proposed, level-set framework was still, however, a relatively “slow” approach especially for 3D or 4D data.

As imaging technology evolves, demands for real-time feedback also increases, mostly for interventional imaging and minimum-invasive surgery. Latest 3D and 4D imaging techniques and real-time imaging techniques not only provide better appreciations of the anatomy and function of the body, but also raise a great challenge for image segmentation in terms of efficiency. In this context, a new framework called Active Geometric Functions (AGF) is proposed in this paper to push the limits of real-time segmentation. AGF is extending implicit representation in the opposite direction as the level-set framework does. Instead of adding one additional dimension to achieve flexibility in topological changes, AGF is achieving benefit in computational efficiency by reducing the dimensionality of the segmentation problem and utilizing efficient function basis. In the following sections, the general AGF framework is proposed and compared to existing deformable model framework. Then, the performance of AGF framework is demonstrated in two cardiac image analysis examples, with an extension to multi-phase segmentation in the second one.

2. General active geometric functions framework

2.1. Interface representation

In image analysis, segmentation refers to the process of partitioning a digital image into multiple segments. Image segmentation is typically used to locate objects and interfaces of these objects (lines, curves, etc.) in images.

In all deformable model methods, interface representation is fundamental. Mathematically, there are two ways to represent the interface:

- Explicit representation: that is representing the surface by explicitly listing the coordinates of the boundary points (i.e. a parametric representation). This is the representation that original snakes [18] used.
- Implicit representation: that is representing the surface by embedding the boundary as the iso-value curves of some function *f* called the representation function. Level-set functions [4–7] are a good example by embedding the interface as the zero level-set of a distance function.

2.2. Geometric function

Most of the recent efforts in segmentation based on implicit interface representation have focused on the level-set framework, given its advantages for topological changes and feasibility to represent convoluted surfaces. As mentioned above, level-set functions add one extra dimension beyond the dimensionality of the image data. For example, to represent a surface in 3D space, the level-set function corresponding to the surface will be a tri-variate function. For comparison, original parametric deformable models only required a list of point coordinates in 3D. For level-set, this extra dimension brings various benefits as well as additional computation load, which may degrade computational efficiency.

By looking the *opposite* way of level-set frameworks, it is very natural to think of dimensionality reduction in surface representation to reduce the computational complexity. Using terminology of interface representation, we are looking for a representation function which has fewer dimensions than the image data, i.e. using a 2D function to represent a 3D surface in space. We call such function a geometric function.

Mathematically, in *N*-dimensional space, we can define a geometric function $g:\mathbb{R}^{N-1} \rightarrow \mathbb{R}$ as a special set of functions representing one of the coordinates constrained by the others. Without losing generality, we can assume that this special coordinate is x_0 and the other coordinates are x_1 to x_{N-1}. That is:

$$x_0 = g(x_1, \ldots, x_{N-1}). \tag{1}$$

The corresponding representation function *f* is defined as

$$f = x_0 = g(x_1, \ldots, x_{N-1}). \tag{2}$$

So that the corresponding boundary is the zero-value curve of the function *f*, i.e. $f = 0$.

Examples of a unit spherical interface represented by different approaches were shown in Fig. 1. Corresponding level-set function (Fig. 1b) as a signed distance function is $\Phi(x, y, z) = \left(1/\sqrt{3}\right)\sqrt{x^2+y^2+z^2} - 1$. And the corresponding geometric function representation (Fig. 1(c)) is $f(r, \theta, \phi) = r - 1 = 0$. Note both implicit functions have the same roots, with the fact that the coordinates used in the explicit representation (Fig. 1(a)) are digitized version of these roots. And geometrically, these roots form the same unit spherical surfaces. This example also illustrates that non-Cartesian coordinate systems can be used in geometric function representation to efficiently represent the desired surfaces.

2.3. Driving forces

Similar to other deformable models, we adopt a variational framework in deriving the driving forces. For example, we can use the Mumford–Shah segmentation energy functional:

$$E\left(F,\vec{C}\right)=\beta\int_{\Omega\setminus\vec{C}}(F-G)^2dV+\alpha\int_{\Omega\setminus\vec{C}}|\nabla F|^2dV+\gamma\oint_{\vec{C}}ds, \tag{3}$$

in which $\vec{C}$ denotes the smoothed and closed segmented interface, G represents the observed image data, F is a piecewise smoothed approximation of G with discontinuities only along $\vec{C}$, and Ω denotes the image domain. Given the flexibility of variational frameworks, other segmentation energy functionals may also be easily adopted.

For the segmentation of an N-dimensional image data set, the Active Geometric Functions framework will solve an $(N-1)$-dimensional variational problem; explicit representation will solve an N-dimensional problem; and the level-set framework will solve an $(N+1)$-dimensional variational problem. It is obvious that AGF framework has advantages in dimensionality reduction when compared with the other two deformable models formulations, at the cost of some flexibility given the assumption of 1 versus $(N-1)$ coordinate mapping. However, such surface mapping can be further modified via the combination with finite element models. In addition, for typical medical applications, biological surfaces are relatively smooth and well represented with relatively simple geometric functions.

2.4. Efficiency of AGF framework

The efficiency benefit of AGFs comes from three aspects: a dimension-reduced surface representation, use of efficient function basis, and dimension reduction of optimization problem. The first two aspects can greatly reduce the number of parameters used in the optimization procedure.

In the general case, for $N-D$ segmentation, let's assume the number of parameters used in parametric models is 1 after normalization, and AGF can gain some parameter reduction factor of r in each dimension by using surface functions and spacing of parametric nodal points of d-pixels in 1D, and narrowband width of level sets is b ($b \geq 3$) in each dimension, then the total number of parameters used in each model is: $(1/d)^{(N-1)}$ for AGF, 1 for parametric model as the reference, and $r^{(N-1)}b^{(N-1)}$ for level sets. In other words, if we use parametric models as the reference method, and represent the computational complexity in terms of the "Big-Oh" representation, then for $N-D$ segmentation, AGF is a $O(-(N-1))$ method in comparison with parametric models and level sets with narrow-banding which is $O(N-1)$ method. The three models are only comparable when $N=2$, in which case $N-1=1$ and level-set and parametric model are different by a linear factor. However, AGF is still two orders of magnitude faster.

With this example, it is clearer of the advantage of AGF in comparison with existing methods, especially for images with higher dimensionality. Nowadays, 3D and 4D image data is becoming routine in medical image analysis and we think that the advantages for AGF in computational efficiency is critical and non-substitutable by existing frameworks.

In general, deformable models usually utilize iterative methods to find the optimal solution for the associated energy minimization framework via curve evolution, which requires an additional variable as an artificial time step added into the functions. In this case, curve

evolution with explicit representation with K node points becomes an $N \times K$ variable minimization problem since the evolving curve is represented by

$$\begin{bmatrix} \vec{X}^0(t) \\ \vec{X}^1(t) \\ \vdots \\ \vec{X}^{K-1}(t) \end{bmatrix} = \begin{bmatrix} x_0^0(t) & x_1^0(t) & \cdots & x_{N-1}^0(t) \\ x_0^1(t) & x_1^1(t) & \cdots & x_{N-1}^1(t) \\ \vdots & \vdots & \vdots & \vdots \\ x_0^{K-1}(t) & x_1^{K-1}(t) & \cdots & x_{N-1}^{K-1}(t) \end{bmatrix}, \tag{4}$$

with $N \times K$ evolving variables.

Curve evolution with level-set becomes an $(N + 1)$-variate functional minimization problem since the evolving curve is represented by

$$\phi\left(\vec{X}, t\right) = \phi\left(x_0, x_1, \ldots, x_{N-1}, t\right), \tag{5}$$

which has to be solved for every point on the entire image domain or within the narrowband.

Curve evolution with surface function actives becomes an N-variate functional minimization problem since the evolving curve can be represented by

$$x_0(t) = f\left(x_1, x_2, \ldots, x_{N-1}, t\right). \tag{6}$$

The advantage in dimensionality reduction for surface function actives over level-set framework is evident.

The advantage of AGF over explicit expression is in two aspects. First, in explicit representation, for each node point, there are N evolving variables, whereas in surface function representation, there is only one variable for each corresponding points. This will become more evident if we digitize Eq. (6) and reformulate in a similar form as in Eq. (4):

$$\begin{bmatrix} \vec{X}^0(t) \\ \vec{X}^1(t) \\ \vdots \\ \vec{X}^{K-1}(t) \end{bmatrix} = \begin{bmatrix} x_0^0(t) & x_1^0 & \cdots & x_{N-1}^0 \\ x_0^1(t) & x_1^1 & \cdots & x_{N-1}^1 \\ \vdots & \vdots & \vdots & \vdots \\ x_0^{K-1}(t) & x_1^{K-1} & \cdots & x_{N-1}^{K-1} \end{bmatrix}. \tag{7}$$

Although the memory usage of Eq. (7) is the same as Eq. (4), the curve evolution of Eq. (7) has $N - 1$ less dimensionality than Eq. (4), which usually leads to faster and more stable convergence. Generally speaking, the more parameters to be optimized, the larger possibility that local minimums and saddle points exist, especially with presence of noise. Of course it is not necessarily true for every case that 1D optimization is more stable than $N - D$; they could be equivalent. But even for that, the searching space for 1D case is much smaller than the $N - D$ one, which leads to faster convergence.

Another aspect is that Eq. (6) can be represented via function basis, such as cubic Hermite functions, in which case only a few weighting parameters rather than a lot of digitized node points have to be stored and iterated on. This can further improve the accuracy, efficiency, and numerical stability.

3. Endocardial segmentation in 4D ultrasound

3.1. Geometric function setup

AGF is a generic framework. The actual geometric function is not necessarily defined on Cartesian bases. Any spatial basis can be chosen for the purpose of efficiency in surface representation. In cardiac applications, given the ellipsoidal shape of the left ventricle, usually spherical coordinate system [19] or prolate spheroidal coordinates system [20] can be used to exploit the shape prior knowledge. Generally in 3D space a geometric function can be described through an equation $v_0 = g(v_1, v_2)$ with coordinates (v_0, v_1, v_2). (v_0, v_1, v_2) can be (r, θ, z) in cylindrical coordinate systems, (r, θ, ϕ) in spherical coordinate systems, and (λ, θ, μ) in prolate spheroidal coordinate systems. In this paper, although prolate spheroidal coordinate systems proposed by Hunter [21] is used, all formulations are expressed in generic form and free of change in coordinate system.

Another benefit of AGF is that it does not require using a single function to represent the entire surface. Piecewise smooth functions building on conceptual patches can be adopted for accuracy and flexibility. Specifically, in this paper, geometric functions described by a conceptual finite element model utilizing cubic Hermite polynomials as geometric function basis was used to efficiently represent the convoluted endocardial surface. The entire endocardial surface was represented by geometric functions built on a "mesh" composed by 8 × 8 conceptual patches. Given the dimensionality reduction of the geometric function representation, on each conceptual patch, a 2D cubic geometric function was defined, using cubic Hermite polynomials as basis functions. On each node of a four-node patch, there were four Hermite coefficients H^i, $i = 1, 2, 3, 4$, controlling the weights of each basis function. Given their efficiency in surface representation, Hermite polynomials are widely used in cardiac biomechanics studies for surface representation [1,22,23]. A simple 8 × 8 finite element model (FEM) with intrinsic C^1 continuity can sufficiently represent the geometry of the endocardium [1,23].In our implementation, this 8 × 8 convention was followed.

3.2. Energy minimization

Following the same rationale used in the Chan and Vese level-set [6] framework, the energy in Eq. (3) can be minimized via a Newton Downhill method:

$$H^{i,t+dt}=H^{i,t} - dt\frac{\partial E}{\partial H^i}, \tag{8}$$

with dt representing the artificial time step in numerical iterations. It has been shown in [20] that for binary segmentation problem, into two partitions $\{\Omega^i\}_{i=1,2}$ of the image domain Ω, $\partial E/\partial H^i$ has the surface integral form of

$$\frac{\partial E}{\partial H^i}=\int_{v_1,v_2}\left(2f^i\left(u-\frac{c_1+c_2}{2}\right)(c_2-c_1)\,V+\upsilon\frac{\partial A}{\partial H^i}\right)dv_1dv_2, \tag{9}$$

with f^i representing the surface coefficient with respect to the basis function values at current surface location, c_1 and c_2 representing the average intensity values in the two partitions, V representing the scaling factor due to coordinate transformation and A representing the surface area. Details on the computation of this term can be found in [20]. The second part in the integration is a curvature term, which is composed by two non-linear terms involving H^i and scaling factors. Due to the intrinsic continuity in the Hermite representation, contribution from this term was usually very small. For this reason, and for cost-

effectiveness, this terms can be either suppressed as proposed in [20] or replaced by an equivalent linear term [19] derived from minimizing curvature instead of the surface area as in the original Chan and Vese framework.

3.3. Results

The proposed method was tested on 35 4D data sets containing 425 frames, acquired by a Philips© iE33 ultrasound machine during five separate canine experiments, with various degrees of induced ischemia as well as controlled stages. Each data set contained 10–15 volumetric frames, depending on the heart rate. Each volume was about 200 × 200 × 200 in matrix size with pixel size of 0.8 mm in each dimension. For quantitative comparison purpose, endocardial borders for all data sets were manually traced by an experienced expert with a computer-aided interface. Eleven data sets were also traced by two other experts to estimate the inter-observer variability. Distances between two surfaces served as quantitative metrics to describe surface discrepancy.

As shown in Fig. 2(a), all 425 segmentation experiments were initialized as a small ellipsoid (defined as an isosurface in prolate spheroidal coordinates) at the center of the image volume and aligned with the vertical direction of the image data, without using any prior knowledge. The segmentation was fully automated without any manual modification. A sample frame overlaying segmentation from AGF (red) and manual tracings from two experts (green and blue) is shown in Fig. 2(b). All three surfaces were very close to each other. This observation was confirmed by quantitative validation. On all 425 frames, the mean distance of AGF segmentation to manual tracing was 4.00 mm (about 3 times the pixel diagonal dimension) with a standard deviation of 3.23 mm; the mean distance between two manual tracings was 4.23 mm with a standard deviation of 3.26 mm.

On average, it took AGF 32.9 ms to converge for one 3D frame, on a regular Pentium 2.0 GHz PC running Redhat Linux, enabling a potentially 33 fps segmentation rate. Note that this rate is faster than the actual imaging acquisition rate (up to 25 Hz), suggesting AGF could enable online segmentation.

4. Myocardial segmentation in high speed MRI

4.1. Coupled active geometric functions

Each AGF model could divide an image into two partitions, i.e. the object (or the foreground) and the background. In order to simultaneously segment multiple objects, similar to level-set framework [19,24,25], more than one deformable model could be introduced at the same time. In order to realize simultaneous multi-object segmentation, these deformable models will be coupled together via some mechanism, such as distance [25] or multi-phase fashion [17,24].

One benefit of implicit surface representation is that the function value of the representation function could be assigned with some physical meanings that may be convenient during segmentation iterations. In level-set framework, usually signed distance functions [4,5] are usually chosen as the level-set function, which not only offers an immediate measures or approximation of the distance to the current interface for any given point, but also have some nice features, such as unitary slope, that would simplified the energy minimization equations. As another implicit surface representation approach, values of Geometric Functions also have physical meanings, i.e. the coordinate values along the direction of one spatial basis functions. These values generally do not correspond to the Euclidean distances for given points to the current surface. However, recalling the definition of coordinate values, it is obvious that this value is a distance measure along the corresponding basis direction. If this basis is linear, the function value is thus a signed distance function, with

some scaling factor, along the basis direction. Moreover, such distance measures usually is an upper bound to the true point-to-surface distance. And sometime it also has clinical importance and diagnostic values. For example, in cardiac diagnosis, radial displacement and radial thickening are important metrics for cardiac dynamics. By choosing a coordinate system with radial directions, such as polar coordinates, Geometric Function values can be immediate measures of radial distance.

This nice feature can also be used in coupling Active Geometric Functions models. Specifically for myocardial segmentation in 2D+ time cine series, two geometric functions can be introduced to simultaneously segment the endocardial and epicardial surfaces. Running this segmentation protocol, both models were driven by forces computed via energy minimization. The total energy was defined by combination of Mumford–Shah energy functionals and a penalty term computed from the signed radial distance between the two surfaces. Specifically, assuming $\overrightarrow{C_1}$ and $\overrightarrow{C_2}$ are the two coupled surfaces with corresponding geometric functions g_1 and g_2, then in polar coordinates system, we had $r = g_1(\theta)$ and $r = g_2(\theta)$. We shall assume $\overrightarrow{C_1}$ targets the endocardial surface and $\overrightarrow{C_2}$ targets epicardial surface. Generally, these two models can divide an image into four different partitions [17,24], with the average intensity values within each partition defined as c_{00}, c_{10}, c_{01}, and c_{11}, as shown in Fig. 3.

Let a function d be a membership penalty function defining a penalty associated with its function variable. In our implementation, a linear penalty function similar to wavelet soft-thresholding [26] function was used. However, more sophisticated membership function such as fuzzy membership function [27] can be used. The membership function was defined as

$$d(x) = \begin{cases} x - d_{\max}, x \geq d_{\max} \\ 0, d_{\min} \leq x \leq d_{\max} \\ x - d_{\min}, x \leq d_{\min} \end{cases}, \tag{10}$$

with d_{min} and d_{max} defining acceptable range of membership. The shape of the membership penalty function is given in Fig. 4. The idea is to penalize large and small values beyond an admissible range of values for the thickness of the myocardium being segmented.

Lastly, a smoothness constraint was superimposed to each AGF model to ensure the papillary muscles were excluded in the endocardial segmentation. In our experiments, since the doctors preferred much smoothed segmentation with papillary muscles excluded, strong smoothness constraints were imposed on both surface functions, resulting circle-like segmentations.

Thus, the final energy functional was defined as

$$
\begin{aligned}
&E\left(F, \overrightarrow{C_1}, \overrightarrow{C_2}\right) \\
&\quad = \lambda_{11} \int_{\substack{inside \quad C_1 \\ inside \quad C_2}} (u - c_{11})^2 \\
&\quad + \lambda_{10} \int_{\substack{inside \quad C_1 \\ outside \quad C_2}} (u - c_{10})^2 \\
&\quad + \lambda_{01} \int_{\substack{outside \quad C_1 \\ intside \quad C_2}} (u - c_{01})^2 \\
&\quad + \lambda_{00} \int_{\substack{outside \quad C_1 \\ outside \quad C_2}} (u - c_{00})^2 \\
&\quad + \gamma_1 \oint_{\overrightarrow{c_1}} ds \\
&\quad + \gamma_2 \oint_{\overrightarrow{c_2}} ds \\
&\quad + \upsilon \oint |d(g_2 - g_1)|^2
\end{aligned}
\tag{11}
$$

with λ_{ij}, $i = 0, 1$; $j = 0, 1$ as the parameters balancing the homogeneity measures, γ_1, γ_2 as the weighting factor for the smoothness constraint for each AGF model, and υ as the parameter controlling the weight for membership penalty.

4.2. Results

The proposed algorithm was applied to 414 frames of clinical Phase Train Imaging (PTI) data with average temporal resolution of 2 milliseconds. Each image frame had a dimension of 160 × 192 pixels. Manual tracing of the endocardium and epicardium was also performed by an experienced expert serving as a gold standard to evaluate the performance of the proposed multi-phase AGF method. The algorithm was preliminarily implemented in Matlab© (The Mathworks, Natick, MA).

The coupled Active Geometric Functions models were automatically initialized as two tiny circles with different radii at the center of the image at the first frame of whole series, as shown in Fig. 5.

After initialization, two AGF models started to evolve under the force derived via energy minimization of the total energy functional defined by Eq. (11) until convergence. The forces from membership penalty functions successfully pushed the outside contour beyond the endocardial surfaces to lock on epicardial surfaces. Subsequently the segmentation results on the current frame were propagated into the next one, utilizing the high temporal resolution that the PTI data offers, followed by curve evolution until convergence and propagation to the next frame. Fig. 5 shows 10 sample frames of the segmentation results taken at different phases of the cardiac cycle. Both endocardial and epicardial surfaces were accurately segmented on all frames with papillary muscle successfully excluded.

The proposed method took 500 ms to segment all 414 frames. On average, it took AGF 6 iterations to reach a stable endocardial and epicardial segmentation with each iteration using

0.194 ms under a Matlab© implementation. All computations were executed on a 2.4 GHz 64-bit AMD server, running Red Hat Linux Enterprise AS. Quantitative evaluations were performed both on endocardial and epicardial segmentation volume, in terms of area difference, true positive fraction, and false positive fraction. For endocardial segmentation, the area difference (mean ± standard deviation) was 8.7 ± 5.9%; the true positive fraction was 93.3 ± 7.0%; and the false positive fraction was 7.0 ± 4.6%. For epicardial segmentation, the area difference was 6.8 ± 5.3%; the true positive fraction was 95.5 ± 3.6%; and the false positive fraction was 7.8 ± 5.2%. Average distance between automated segmented surfaces and manually traced surfaces was 3.0 ± 2.4 pixels. Comparison metrics from a recent systematic study on cardiac MRI segmentation [24] were used as a reference, which suggested that our results were comparable to level-set-based methods as well as inter-observer variance. Note that the PTI images have slightly coarser resolution as well as a slightly blurrier appearance than regular cardiac cine MRI due to undersampling in the phase-encoding direction, which may increase the inter-observer variance as reported in [24].

5. Conclusions

Active Geometric Functions (AGF) was presented as a new framework for deformable model. It was demonstrated in two cardiac applications: endocardial segmentation in 4D ultrasound and myocardial segmentation in MRI with super high temporal resolution. In both applications, AGF could perform real-time segmentation in several milliseconds per frame, which was less than the acquisition time per frame. Segmentation results were compared to manual tracing with comparable performance with inter-observer variability. AGF offered great advantages in computational efficiency, benefiting from dimensionality reduction in the interface representation. It utilized implicit surface representation, enabling easy determination of inside and outside surface areas as well as straightforward quantitative segmentation comparison. Moreover, besides providing numerical solutions to the desired interface like a level-set framework, AGF could use closed form expressions as well as achieve even better efficiency and accuracy. The continuous form of interface function could also benefit downstream analysis based on shape or other information from the interface. AGF was suitable for any applications where real-time feedback is desired, such as interventional procedure or online segmentation. The variational framework that AGF adopted provides flexibility of further expansion in terms of additional constraints or the ability to deal with multi-channel multi-phase segmentation problems. And, AGF can easily utilize more complex energy functions that have been proposed (e.g. conditional random fields) in place of the original Mumford–Shah style functions, to achieve better performance in image segmentation.

references

1. Herz S, Ingrassia C, Homma S, et al. Parameterization of left ventricular wall motion for detection of regional ischemia. Annals of Biomedical Engineering. 2005; 33(7):912–919. [PubMed: 16060531]
2. Udupa JK, Wei L, Samarasekera S, et al. Multiple sclerosis lesion quantification using fuzzy connectedness principles. IEEE Transactions in Medical Imaging. 1997; 16:598–609.
3. Kass M, Witkin A, Terzopoulos D. Snakes: active contour models. International Journal of Computer Vision. 1987; 1:321–331.
4. Sethian, J. Level Set Methods and Fast Marching Methods. 2 ed.. Vol. 3. Cambridge University Press; Cambridge: 1999.
5. Osher, S.; Fedkiw, R. Level Set Methods and Dynamic Implicit Surfaces. Vol. 153. Springer; New York: 2003.

6. Chan TF, Vese LA. Active contours without edges. IEEE Transactions on Image Processing. 2001; 10(2):266–277. [PubMed: 18249617]
7. Angelini E, Homma S, Pearson G, et al. Segmentation of real-time three-dimensional ultrasound for quantification of ventricular function: a clinical study on right and left ventricles. Ultrasound in Medicine and Biology. 2005; 31(9):1143–1158. [PubMed: 16176781]
8. Cootes TF, Taylor CJ, Cooper DH, et al. Active shape models—their training and application. Computer Vision and Image Understanding. 1995; 61(1):38–59.
9. Cootes, TF.; Edwards, GJ.; Taylor, CJ. Active appearance models, in: Lecture Notes in Computer Science. Vol. 1407. Springer; Berlin/Heidelberg: 1998. p. 484-498.
10. Held K, Kops ER, Krause BJ, et al. Markov random field segmentation of brain MR images. IEEE Transactions in Medical Imaging. 1997; 16(6):878–886.
11. Boykov, YY.; Jolly, M-P. Interactive graph cuts for optimal boundary & region segmentation of objects; N − D Images in Eighth International Conference on Computer Vision (ICCV'01); 2001. p. 105-112.
12. Jin, Y.; Imielinska, C.; Laine, A., et al. Segmentation and evaluation of adipose tissue from whole body MRI scans; Proceedings of the Sixth International Conference on Medical Image Computing and Computer Assisted Interventions (MICCAI 2003); Montreal Canada. 2003. p. 635-642.
13. Xu C, Prince JL. Snakes, shapes and gradient vector flow. IEEE Transaction on Image Processing. 1998; 7(3):359–369.
14. Sethian, JA. Level Set Methods and Fast Marching Methods: Evolving Interfaces in Computational Geometry, Fluid Mechanics, Computer Vision, and Materials Science. Cambridge University Press; Cambridge, UK: 1999.
15. Mumford, D.; Shah, J. Boundary detection by minimizing functional; International Conference on Computer Vision and Pattern Recognition; San Francisco, CA, USA. 1985. p. 22-26.
16. Angelini E, Laine A, Takuma S, et al. LV volume quantification via spatio-temporal analysis of real-time 3D echocardiography. IEEE Transactions on Medical Imaging. 2001; 20(6):457–469. [PubMed: 11437106]
17. Song, T.; Angelini, ED.; Mensh, BD., et al. Comparison study of clinical 3D MRI brain segmentation evaluation; Annual International Conference IEEE Engineering in Medicine and Biology Society (EMBS); San Francisco, CA, USA. 2004. p. 1671-1674.
18. Kass, M.; Witkin, A.; Terzopoulos, D. Snakes: active contour models; Proceedings of 1st International Conferences on Computer Vision; 1987. p. 259-268.
19. Duan, Q.; Shechter, G.; Gutierrez, LF., et al. Augmenting CT cardiac roadmaps with segmented streaming ultrasound; SPIE International Symposium, Medical Imaging 2007; San Diego, CA. 2007. p. 65090V1-65111V.
20. Vallet, B.; Angelini, E.; Laine, A. Variational segmentation framework in prolate spheroidal coordinates for 3D real-time echocardiography; SPIE Medical Imaging Conference; San Diego, CA, USA. 2006. p. 61444A.1-61511A.
21. Hunter PJ, Smaill BH. The analysis of cardiac function: a continuum approach. Progress in Biophysics and Molecular Biology. 1988; 52:101–164. [PubMed: 3076684]
22. Christie GR, Bullivant DP, Blackett SA, et al. Modelling and visualising the heart. Computing and Visualization in Science. 2004; 4(4):227–235.
23. Nielsen PM, LeGrice IJ, Smaill BH, et al. Mathematical model of geometry and fibrous structure of the heart. American Journal of Physiology—Heart and Circulation Physiology. 1991; 260:H1365–H1378.
24. Angelini ED, Song T, Mensh BD, et al. Brain MRI segmentation with multiphase minimal partitioning: a comparative study. International Journal of Biomedical Imaging. 2006; 2007:1–15. Article ID 10526.
25. Zeng X, Staib LH, Schultz RT, et al. Segmentation and measurement of the cortex from 3-D MR images using coupled-surfaces propagation. IEEE Transactions on Medical Imaging. 1999; 18(10): 927–937. [PubMed: 10628952]
26. Jin, Y.; Angelini, E.; Laine, A. Wavelets in medical image processing: denoising, segmentation, and registration. In: Suri, J.; Wilson, DL.; Laximinarayan, S., editors. Handbook of Medical Image

Analysis: Advanced Segmentation and Registration Models. Kluwer Academic Publishers; New York, NY: 2004.

27. Udupa JK, Samarasekera S. Fuzzy connectedness and object definition: theory, algorithms, and applications in image segmentation. Graphical Models and Image Processing. 1996; 58(3):246–261.

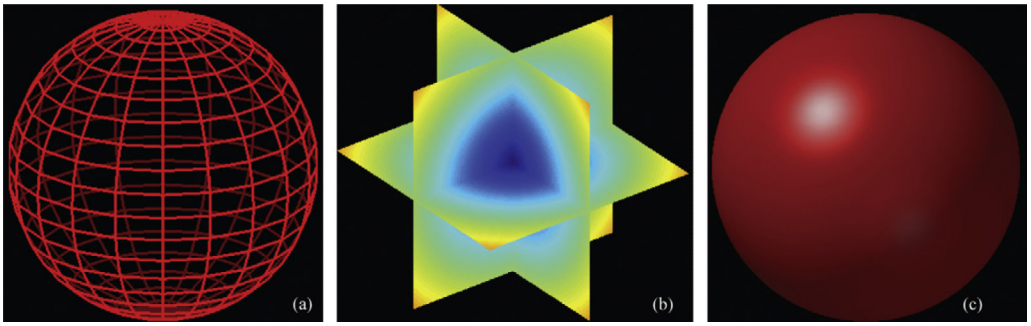

Fig. 1.
Surface representations using (a) explicit representation, (b) level-set framework, and (c) geometric functions.

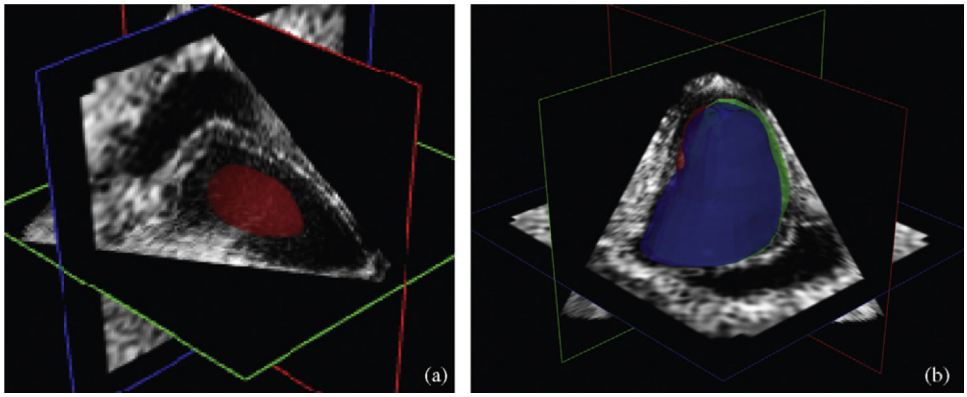

Fig. 2.

(a) Automatic initialization of the LV surface with an ellipsoid positioned at the center of the volume; (b) overlaid segmentation results from AGF (red), one expert (green), and the other expert (blue). All three surfaces were very close to each other. (For interpretation of the references to color in this figure legend, the reader is referred to the web version of the article.)

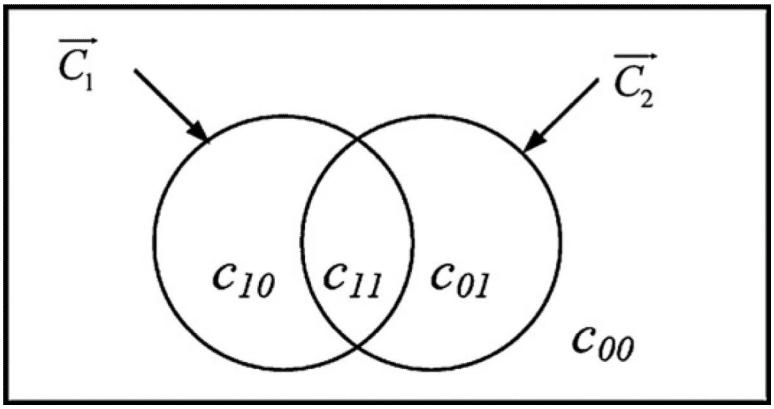

Fig. 3.
Partitioning of the image into four phases using two level-set functions. Average intensity values are designed as c_{00}, c_{10}, c_{01}, c_{11}.

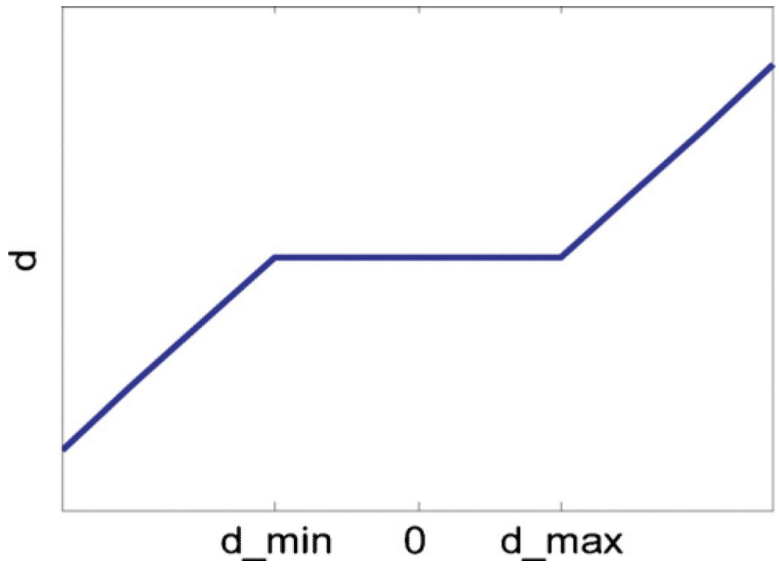

Fig. 4.
Shape of membership penalty function.

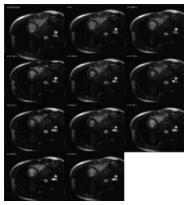

Fig. 5.
Illustration of initialization at the first frame and segmentation of endocardium and epicardium on 10 frames out of 414 frames. The red curves indicate the automated endocardium segmentation; the green ones are automated epicardium segmentation.